

The characterization of plastic flow in three different bulk metallic glass systems

Dongmei Xing^{a,b}, Taihua Zhang^{a,*}, Weihuo Li^c, Bingchen Wei^c

^a State Key Laboratory of Nonlinear Mechanics (LNM), Institute of Mechanics, Chinese Academy of Sciences, Beijing 100080, PR China

^b College of Physics and Electronic Information Science, Tianjin Normal University, Tianjin 300072, PR China

^c National Microgravity Laboratory, Institute of Mechanics, Chinese Academy of Sciences, Beijing 100080, PR China

Received 12 January 2006; received in revised form 19 June 2006; accepted 21 June 2006

Available online 31 July 2006

Abstract

Plastic deformation behaviors of $\text{Zr}_{52.5}\text{Al}_{10}\text{Ni}_{10}\text{Cu}_{15}\text{Be}_{12.5}$, $\text{Mg}_{65}\text{Cu}_{25}\text{Gd}_{10}$ and $\text{Pd}_{43}\text{Ni}_{10}\text{Cu}_{27}\text{P}_{20}$ bulk metallic glasses (BMGs) are studied by using the depth-sensing nanoindentation, macroindentation and uniaxial compression. The significant difference in plastic deformation behavior cannot be correlated to the Poisson's ratio or the ratio of shear modulus to bulk modulus of the three BMGs, but can be explained by the free volume model. It is shown that the nucleation of local shear band is easy and multiple shear bands can be activated in the $\text{Zr}_{52.5}\text{Al}_{10}\text{Ni}_{10}\text{Cu}_{15}\text{Be}_{12.5}$ alloy, which exhibits a distinct plastic strain during uniaxial compression and less serrated flow during nanoindentation.

© 2006 Elsevier B.V. All rights reserved.

Keywords: Bulk metallic glass; Plastic deformation; Shear band; Nanoindentation

1. Introduction

It is well known that plastic deformation in metallic glass alloys at low temperatures ($T < 0.7T_g$) is due to the propagation of shear bands [1]. All bulk metallic glasses (BMGs) show near-zero ductility in tension, under which loading a sample fails following the propagation of a single shear band [2,3]. In constrained modes of loading (e.g., compression or bending), global plastic deformation at room temperature is possible [4–8]. The degree of plastic deformation before failure differs widely from composition to composition. Some BMGs (e.g., Zr-, Pt- and Pd-based BMGs) show distinct plasticity under compression and bending, with the associated fracture surface showing a very characteristic vein pattern and evidence of high local plasticity arising from instabilities in the band of lowered viscosity. In contrast, other BMGs (e.g., Mg- and Fe-based BMGs) are both globally and locally brittle, showing quite different fracture surfaces and notch toughness less than $5 \text{ MPa m}^{1/2}$ [9–11]. Lewandowski et al. has correlated the intrinsic plasticity or brittleness of BMGs with elastic properties, where BMGs are

intrinsically brittle for the ratio of the elastic shear modulus to the bulk modulus (μ/B) > 0.41 – 0.43 , or equivalently for the Poisson's ratio (ν) < 0.31 – 0.32 [12].

A direct comparison of the plastic deformation behavior in brittle and non-brittle BMGs will be interesting for a further understanding of the instinct brittleness or plasticity of metallic glasses. However, up to now there is quite less information available on this field due to the very limited plastic strain in many brittle BMG systems during macroscopic property measurements. Recently, indentation experiments are increasingly being used to evaluate the mechanical response of metallic glasses, due to that considerably larger plastic deformation can be accumulated in these quasi-brittle materials in a localized area around the indented regions [13–16]. Moreover, much mechanical information can be collected from the same sample, which not only greatly reduces the effort for sample preparation but also reduces the sample for sample variation in property. Such factors facilitate observation of the mechanisms of plastic deformation under well-controlled conditions. In this work, we studied the plastic deformation behavior and shear banding features in three BMGs with quite different macroscopic plasticity through nanoindentation and macroindentation. The free volume model was used to describe the plastic flow feature in the alloys.

* Corresponding author. Tel.: +86 10 62541733.

E-mail address: Zhangth@lnm.imech.ac.cn (T. Zhang).

2. Experimental procedure

Cylindrical rods of $\text{Zr}_{52.5}\text{Al}_{10}\text{Ni}_{10}\text{Cu}_{15}\text{Be}_{12.5}$ and $\text{Pd}_{43}\text{Ni}_{10}\text{Cu}_{27}\text{P}_{20}$ alloys with 3 mm diameter were prepared by melting pure metals in an argon atmosphere and suction-casting in a copper mold. $\text{Mg}_{65}\text{Cu}_{25}\text{Gd}_{10}$ rod with 5 mm diameter was processed by melting pure Mg with intermediate Cu–Gd alloy and chill-casting in a copper mold. Structural characterization was done by X-ray diffraction (XRD), which proved the amorphous structure of the as-cast specimens (not shown here). The uniaxial compressive tests on cylindrical samples of 3 mm in diameter and 6 mm in length were performed in a commercial Instron-type testing machine at room temperature. The crosshead was moved at a constant speed with an initial strain rate of $1.0 \times 10^{-4} \text{ s}^{-1}$.

The specimens for nanoindentation measurements were mechanically polished to a mirror finish and tested in a MTS Nano Indenter[®] XP with a Berkovich diamond tip. The indentations were performed in load-control mode to a depth limit of $1 \mu\text{m}$ using loading rates from 0.075 to 5 mN/s. At least six indentations were made for each test. The subsurface deformation morphology was checked with the bonded interface technique [17]. The two mirror polished surfaces were bonded using a high strength adhesive. A careful bonding was made to minimize the bond layer thickness less than $5 \mu\text{m}$. The macro-indentation tests were performed with Vickers indenter on the bonded interface as well as away from it. The indenter was attached to a load cell that was bolted to the bottom of the crosshead of an Instron 5848 Microforce Tester. The indentation measurements were performed in a displacement-control mode to a load limit of 10 N with the loading rate from 15 to 1000 nm/s. After the measurements, the bonded interface was opened subsequently by dissolving the adhesive in acetone. Deformation zones observations were performed using a JSM-6400 scanning electron microscopy (SEM).

3. Results and discussion

Fig. 1 shows the compressive stress–strain curves of three BMGs, measured at the initial strain rate of $1.0 \times 10^{-4} \text{ s}^{-1}$. $\text{Zr}_{52.5}\text{Al}_{10}\text{Ni}_{10}\text{Cu}_{15}\text{Be}_{12.5}$ BMG exhibits elastic limit of 1.7%, yield strength of 1780 MPa, and a large compressive plastic strain of about 5.3%. $\text{Pd}_{43}\text{Ni}_{10}\text{Cu}_{27}\text{P}_{20}$ and $\text{Mg}_{65}\text{Cu}_{25}\text{Gd}_{10}$ BMGs exhibit elastic limit of about 1.6% and 1.3%, respectively, and no global plasticity. The compressive properties of the alloys are summarized in Table 1. The shear modulus (μ), bulk modulus (B) and Poisson's ratio (ν) of the three BMGs taken from Refs. [18–20] are also listed in Table 1. The ν values of $\text{Zr}_{52.5}\text{Al}_{10}\text{Ni}_{10}\text{Cu}_{15}\text{Be}_{12.5}$, $\text{Mg}_{65}\text{Cu}_{25}\text{Gd}_{10}$ and $\text{Pd}_{43}\text{Ni}_{10}\text{Cu}_{27}\text{P}_{20}$ BMGs are 0.356, 0.399 and 0.32, respectively. While, the ratio of μ/B is 0.32 for $\text{Zr}_{52.5}\text{Al}_{10}\text{Ni}_{10}\text{Cu}_{15}\text{Be}_{12.5}$ BMG, 0.42 for $\text{Mg}_{65}\text{Cu}_{25}\text{Gd}_{10}$ BMG and 0.22 for $\text{Pd}_{43}\text{Ni}_{10}\text{Cu}_{27}\text{P}_{20}$ BMGs. It can be found from Table 1 that the $\text{Zr}_{52.5}\text{Al}_{10}\text{Ni}_{10}\text{Cu}_{15}\text{Be}_{12.5}$ BMG with distinct plastic strain during compression exhibits a medium value of ν and μ/B , while $\text{Pd}_{43}\text{Ni}_{10}\text{Cu}_{27}\text{P}_{20}$ BMG exhibits the highest ν

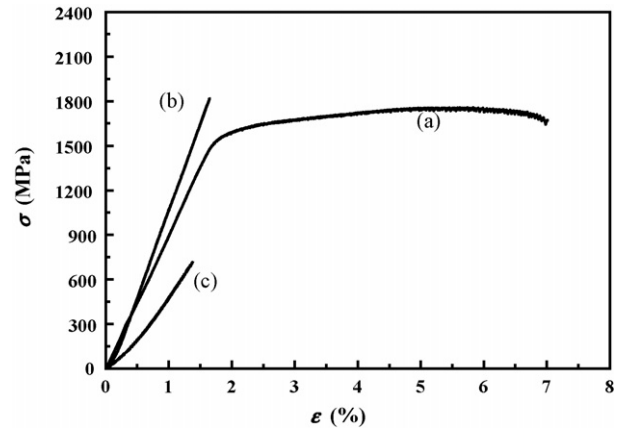


Fig. 1. Stress–strain curves of (a) $\text{Zr}_{52.5}\text{Al}_{10}\text{Ni}_{10}\text{Cu}_{15}\text{Be}_{12.5}$, (b) $\text{Pd}_{43}\text{Ni}_{10}\text{Cu}_{27}\text{P}_{20}$ and (c) $\text{Mg}_{65}\text{Cu}_{25}\text{Gd}_{10}$ BMGs under compression at the strain rate of $1.0 \times 10^{-4} \text{ s}^{-1}$.

value and the lowest μ/B value among the three BMGs. More recently, the flow and fracture mechanism of metallic glasses has been correlated to the ratio of μ/B or ν value [12,21]. The low energy of fracture is related to the high elastic modulus ratio μ/B or the low elastic constant ν , and metallic glasses with $\mu/B > 0.41$ – 0.43 (or, equivalently with $\nu < 0.31$ – 0.32) are intrinsic brittle. However, in this work, the plasticity of the BMGs does not exhibit a general correlation to the μ/B or ν value. The $\text{Zr}_{52.5}\text{Al}_{10}\text{Ni}_{10}\text{Cu}_{15}\text{Be}_{12.5}$ BMG with a medium μ/B ratio of 0.32 and ν value of 0.356 exhibits the highest plasticity during compression, and the other two BMGs show almost no global plasticity. To compare the plastic deformation process in these alloys with quite different plasticity, we studied the deformation behaviors in these alloys during nanoindentation.

Load–displacement (P – h) curves of the three BMGs during the nanoindentation at the loading rate from 0.075 to 5.0 mN/s are shown in Fig. 2. In this figure, the origin of each curve has been displaced such that multiple curves can be accommodated on each graph. Three BMGs exhibit the serrated flow depending on the loading rate in the loading process of indentation. Slow indentation rates promote more conspicuous serrations, and rapid indentations suppress the serrated flow. The critical loading rates for the disappearance of the serrated flow in $\text{Zr}_{52.5}\text{Al}_{10}\text{Ni}_{10}\text{Cu}_{15}\text{Be}_{12.5}$, $\text{Pd}_{43}\text{Ni}_{10}\text{Cu}_{27}\text{P}_{20}$ and $\text{Mg}_{65}\text{Cu}_{25}\text{Gd}_{10}$ are 0.075, 1.0 and 1.0 mN/s, respectively. Schuh and Nieh proposed that serrations are associated with the operation of a single shear band at low rates, while multiple

Table 1

The mechanical properties of amorphous $\text{Zr}_{52.5}\text{Al}_{10}\text{Ni}_{10}\text{Cu}_{15}\text{Be}_{12.5}$, $\text{Pd}_{43}\text{Ni}_{10}\text{Cu}_{27}\text{P}_{20}$ and $\text{Mg}_{65}\text{Cu}_{25}\text{Gd}_{10}$ alloys

| Material properties | $\text{Zr}_{52.5}\text{Al}_{10}\text{Ni}_{10}\text{Cu}_{15}\text{Be}_{12.5}$ | $\text{Pd}_{43}\text{Ni}_{10}\text{Cu}_{27}\text{P}_{20}$ | $\text{Mg}_{65}\text{Cu}_{25}\text{Gd}_{10}$ |
|---|--|---|--|
| σ_y (MPa) | 1780 | 1816 | 528 |
| Elastic strain (%) | 1.7 | 1.6 | 1.3 |
| Plastic strain (%) | 5.3 | 0 | 0 |
| Young's modulus, E (GPa) ^a | 95.7 | 123.1 | 50.6 |
| Poisson's ratio, ν^a | 0.356 | 0.399 | 0.32 |
| Shear modulus, μ (GPa) ^a | 35.3 | 34.5 | 19.3 |
| Bulk modulus, B (GPa) ^a | 110.5 | 160.1 | 45.1 |

^a Data from Refs. [18–20].

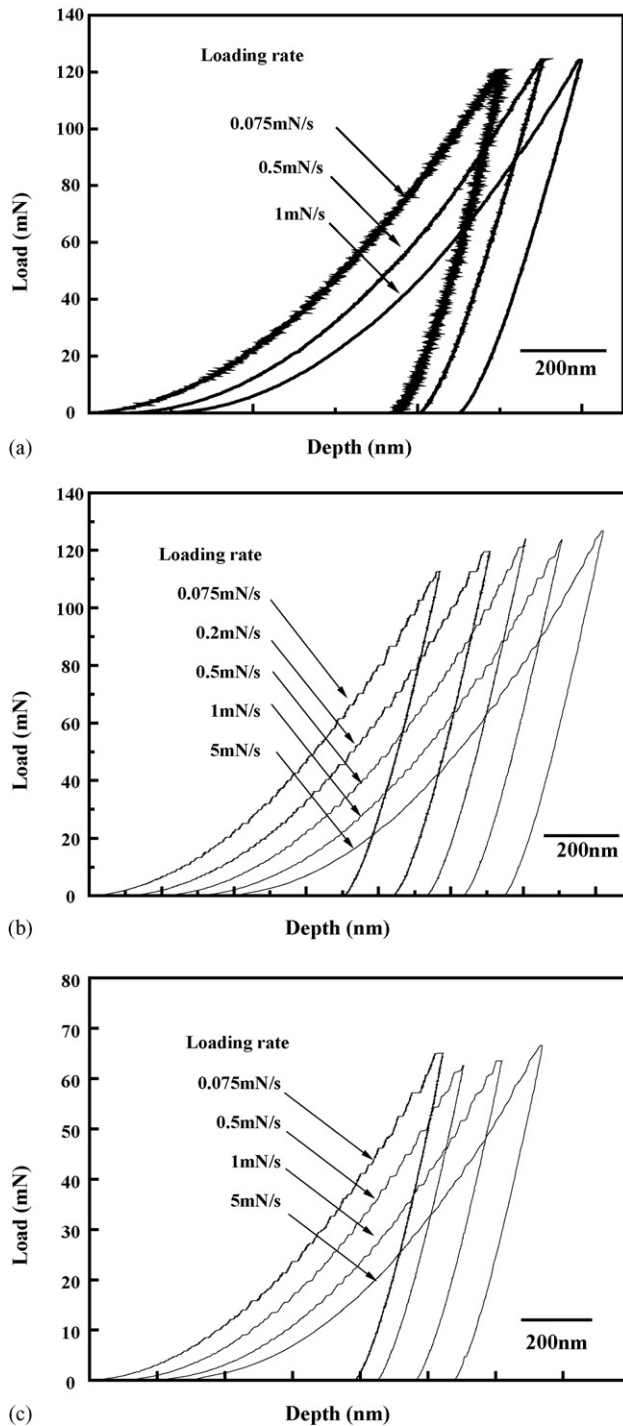


Fig. 2. The typical load–displacement (P – h) curves during nanoindentation measured on at different loading rates for (a) $\text{Zr}_{52.5}\text{Al}_{10}\text{Ni}_{10}\text{Cu}_{15}\text{Be}_{12.5}$ BMG, (b) $\text{Pd}_{43}\text{Ni}_{10}\text{Cu}_{27}\text{P}_{20}$ BMG and (c) $\text{Mg}_{65}\text{Cu}_{25}\text{Gd}_{10}$ BMG. Curves are offset from origin for clear viewing.

shear bands are activated simultaneously at higher rates [22]. The much lower critical loading rates for the disappearance in the $\text{Zr}_{52.5}\text{Al}_{10}\text{Ni}_{10}\text{Cu}_{15}\text{Be}_{12.5}$ BMG than that in the other two BMGs indicates that the nucleation of multiple shear bands is easier in $\text{Zr}_{52.5}\text{Al}_{10}\text{Ni}_{10}\text{Cu}_{15}\text{Be}_{12.5}$ alloy. Moreover, the average magnitude and number of serrations obviously are different in the three BMGs at the same loading rate. The number of

serrations in $\text{Zr}_{52.5}\text{Al}_{10}\text{Ni}_{10}\text{Cu}_{15}\text{Be}_{12.5}$ is higher than that in the other two BMGs. At the indentation depth of 800–900 nm and at the loading rate of 0.075 mN/s, the average magnitudes of serrations in $\text{Zr}_{52.5}\text{Al}_{10}\text{Ni}_{10}\text{Cu}_{15}\text{Be}_{12.5}$, $\text{Pd}_{43}\text{Ni}_{10}\text{Cu}_{27}\text{P}_{20}$ and $\text{Mg}_{65}\text{Cu}_{25}\text{Gd}_{10}$ are 6.1, 14.8 and 13.1 nm, respectively. The appearance of more serrations with smaller magnitude in $\text{Zr}_{52.5}\text{Al}_{10}\text{Ni}_{10}\text{Cu}_{15}\text{Be}_{12.5}$ BMG during nanoindentation suggests the easier nucleation of multiple shear bands during plastic deformation. In contrast, single shear bands can propagate sufficiently in the Mg- and Pd-based BMGs, which lead to the prominent serrations with large size. The serrated flow feature of the Mg- and Pd-based BMGs during nanoindentation agrees well with the results of BMGs with similar chemical composition.

To characterize the shear banding feature of the three BMGs after indentation, we studied the deformation region underneath the Vickers indenter employing the bonded interface technique. Fig. 3 shows deformation region underneath the indenter for three BMGs at the applied indentation load of 10 N and the loading rate of 15 nm/s. The deformation zone of all the three BMGs is hemispherical in nature containing a high density of shear bands. Both semi-circular and radial shear bands can be identified within the deformed zone, and the previous ones are dominated. Fig. 4 summarizes the variation of the inter-band spacing for the semi-circular bands, φ , as a function of radial distance away from the indenter tip, χ , for three BMGs at different loading rates. For $\text{Zr}_{52.5}\text{Al}_{10}\text{Ni}_{10}\text{Cu}_{15}\text{Be}_{12.5}$ BMG, φ is constant with respect to χ , exhibiting an average spacing of 0.87 μm at loading rate of 15 nm/s. In contrast, φ varies strongly with χ in $\text{Mg}_{65}\text{Cu}_{25}\text{Gd}_{10}$ BMG, increasing from 0.96 μm at close to the indenter to a spacing of 7.94 μm for the outmost bands. In the case of $\text{Pd}_{43}\text{Ni}_{10}\text{Cu}_{27}\text{P}_{20}$ BMG, φ shows a weak dependency on χ , increasing from about 0.65 μm to about 1.98 μm . The average inter-band spacing in Zr-, Pd- and Mg-based BMGs is 0.87, 0.99 and 4.06 μm , respectively, at the loading rate of 15 nm/s. This indicates that the high plasticity during compression (Fig. 1) and the less pronounced serrations during nanoindentation (Fig. 2) in $\text{Zr}_{52.5}\text{Al}_{10}\text{Ni}_{10}\text{Cu}_{15}\text{Be}_{12.5}$ BMG correlate with the formation of high density of shear bands during plastic deformation. It can also be seen from Fig. 4 that φ decreases with increasing loading rate for all the three BMGs. In $\text{Zr}_{52.5}\text{Al}_{10}\text{Ni}_{10}\text{Cu}_{15}\text{Be}_{12.5}$ BMG the average spacing is 0.87 and 0.75 μm at the loading rate of 15 and 1000 nm/s, respectively. While for the brittle $\text{Mg}_{65}\text{Cu}_{25}\text{Gd}_{10}$ BMG, φ is more sensitive to the loading rate, and decreases from 4.06 to 2.36 μm as the loading rate increases from 15 to 1000 nm/s.

To gain further insights into the differences in the plastic deformation behavior of the three BMGs, we turn to the free volume theory, in which the formation of shear bands in metallic glasses is mainly due to the creation and coalescence of free volume in some local regions. Assuming that the metallic glass behaves homogeneously in shear band region, the shear strain rate is given by Ref. [23]:

$$\frac{\partial \gamma}{\partial t} = \frac{\dot{\epsilon}}{\mu} + 2f \exp \left[-\frac{\alpha}{\xi} - \frac{\Delta G_m}{k_B T} \right] \sinh \left(\frac{\tau \Omega}{2k_B T} \right) \quad (1)$$

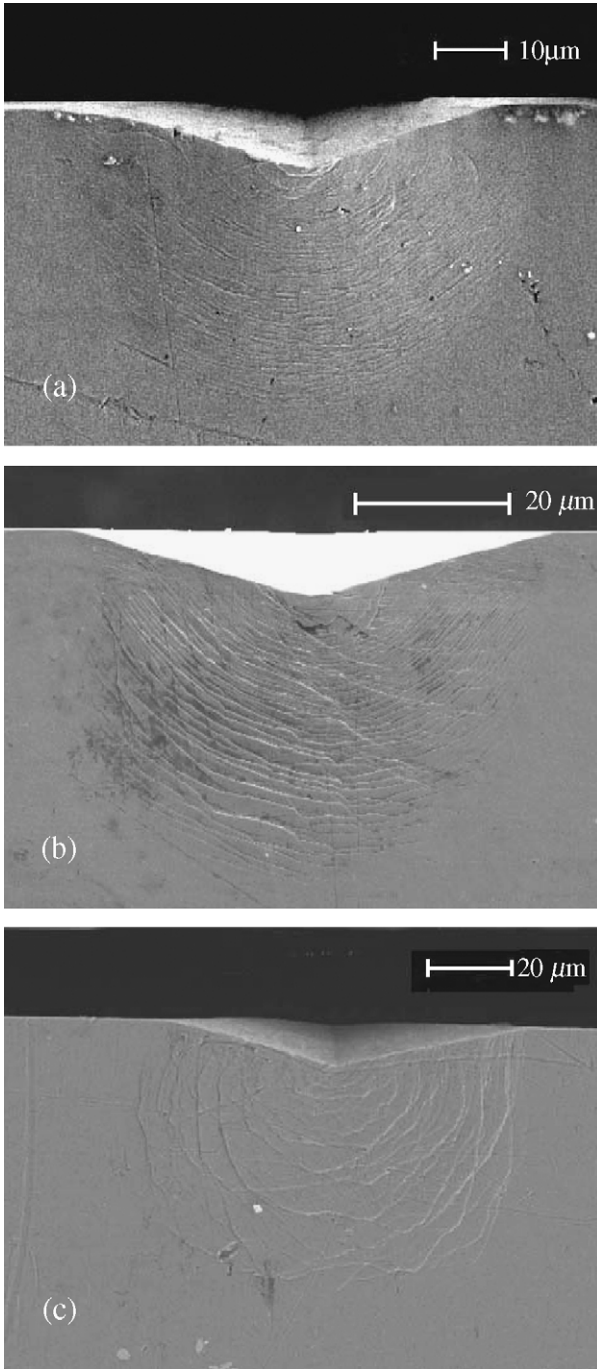


Fig. 3. Morphology of the subsurface plastic deformation zones after macroindentation for two bulk metallic glasses underneath the Vickers indenter: (a) $\text{Zr}_{52.5}\text{Al}_{10}\text{Ni}_{10}\text{Cu}_{15}\text{Be}_{12.5}$ BMG, (b) $\text{Pd}_{43}\text{Ni}_{10}\text{Cu}_{27}\text{P}_{20}$ BMG and (c) $\text{Mg}_{65}\text{Cu}_{25}\text{Gd}_{10}$ BMG the loading rate of 15 nm/s and maximum load of 10 N.

where $\partial\gamma/\partial t$ is the constant shear strain rate, $\dot{\tau}$ the rate of change of the applied stress, ξ the concentration of free volume defined by $\xi = v_f/v^*$ (where v_f the average free volume per atom and v^* a critical volume), α a geometrical factor, f the frequency of atomic vibration, ΔG_m the activation energy, Ω the atomic volume, k_B the Boltzmann's constant and T is the absolute temperature. According to Spaepen [24], free volume is created by an applied shear stress τ and annihilated by a series of atomic jumps, the

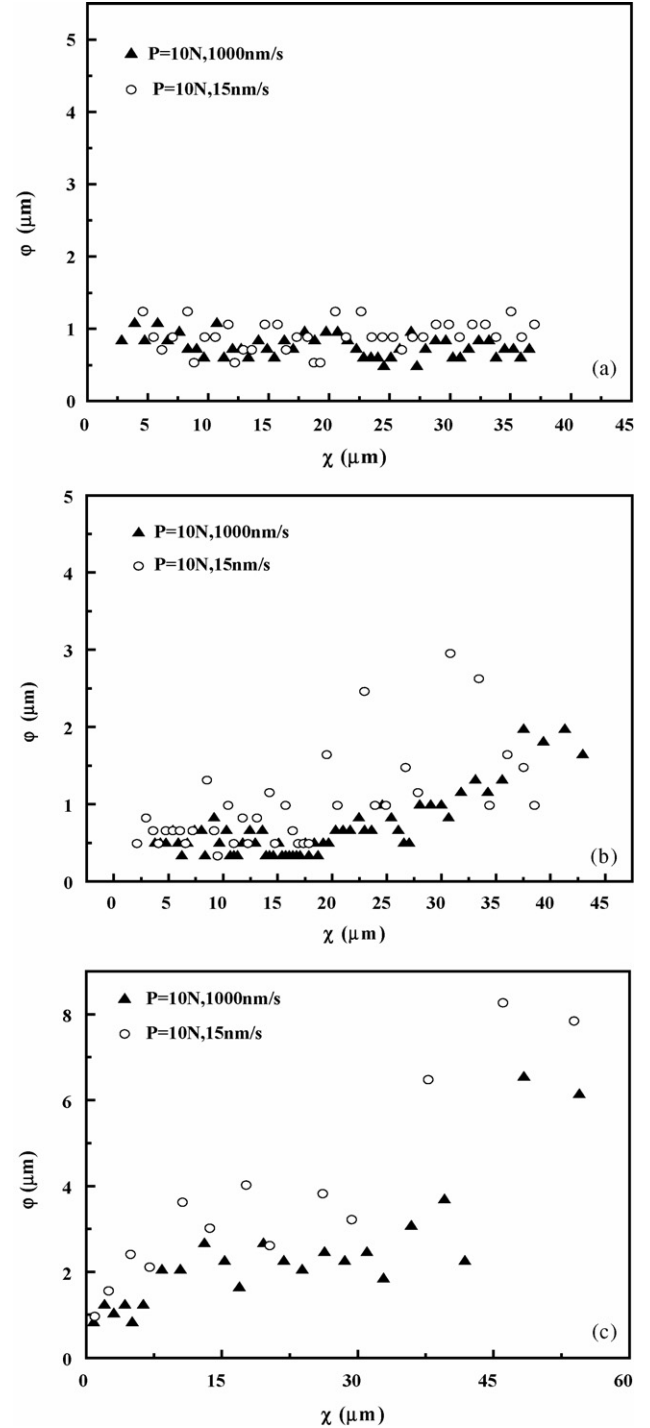


Fig. 4. Variation of the inter-band spacing as a function of distance from the indenter tip, for (a) $\text{Zr}_{52.5}\text{Al}_{10}\text{Ni}_{10}\text{Cu}_{15}\text{Be}_{12.5}$ BMG, (b) $\text{Pd}_{43}\text{Ni}_{10}\text{Cu}_{27}\text{P}_{20}$ BMG and (c) $\text{Mg}_{65}\text{Cu}_{25}\text{Gd}_{10}$ BMG at different loading rates and different maximum loads.

net rate of change of the free volume concentration, $\dot{\xi}$, given by [23]:

$$\frac{\partial \xi}{\partial t} = f \exp \left[-\frac{\alpha}{\xi} - \frac{\Delta G_m}{k_B T} \right] \left\{ -\frac{2\alpha k_B T}{S \xi v^*} \left(\cosh \frac{\tau \Omega}{2 k_B T} - 1 \right) - \frac{1}{n_D} \right\} \quad (2)$$

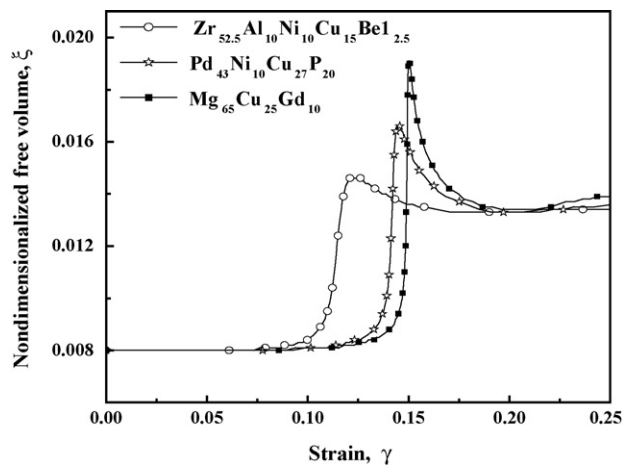


Fig. 5. Plots of the concentration of free volume vs. strain for three BMGs.

where n_D is the number of atomic jumps required to annihilate v^* , $S = 2/3(1 + \nu/1 - \nu\mu)$, ν the Poisson's ratio, and μ is the shear modulus.

Eqs. (1) and (2) are solved numerically with the initial conditions $\tau(t=0) = 0$ and $\xi(t=0) \approx 0.008$. The relevant constants used for three BMGs are taken from Refs. [18–20]. Fig. 5 illuminates the concentration of free volume versus strain for three BMGs at the same loading condition. It can be seen that the free volume concentration increases dramatically at certain critical strain for all the three BMGs. The critical strain in $\text{Zr}_{52.5}\text{Al}_{10}\text{Ni}_{10}\text{Cu}_{15}\text{Be}_{12.5}$ alloy is much lower than that in the other two BMGs. Furthermore, the peak values of free volume concentration in $\text{Zr}_{52.5}\text{Al}_{10}\text{Ni}_{10}\text{Cu}_{15}\text{Be}_{12.5}$ alloy is also much lower than that in the Mg- and Pd-based BMGs. This proves that the nucleation of shear bands and the activation of multiple shear bands are easier during plastic deformation in the Zr-based BMG. The easier activation of multiple shear bands deduced from the free volume model is consistent with the high number density of shear bands underneath the indenter (Figs. 3 and 4), and the low magnitude of serrations during nanoindentation (Fig. 2), as well as the high plastic strain during compressive tests (Fig. 1) in the Zr-based BMG. In contrast, the nucleation of shear bands is difficult in the Mg- and Pd-based BMGs, and the propagation of a single shear band is easy in these alloys due to the higher peak value of the free volume. The difficulty in the nucleation of shear bands is responsible for the prominent serrated flow during nanoindentation (Fig. 2) and the premature fracture during compression (Fig. 1) in the Mg- and Pd-based BMGs. In addition, by comparing the Pd-based BMG with the Mg-based BMG, we can see that the Pd-based BMG has a lower critical strain for the formation of shear bands than Mg-based BMG (Fig. 5). This indicates that the Pd-based BMG has a higher intrinsic plasticity than the Mg-based BMG due to the relatively easier nucleation of shear bands, though both alloys show no global plastic strain during compressive tests (Fig. 1). This point is also proved by the lower inter-band spacing in the Pd-based BMG (Fig. 3b and c). The higher concentration of free volume due to the formation of shear bands in the Mg-based BMG (Fig. 5) may also give rise to a strong

stress relaxation in the vicinity of shear bands [25], resulting in a larger shear band spacing during plastic deformation. This case is more prominent at the locations far from the indenter due to the decrease of stress gradient [26], and tends to form shear bands with much larger spacing in the Mg-based BMG.

4. Conclusion

Plastic deformation behaviors of $\text{Zr}_{52.5}\text{Al}_{10}\text{Ni}_{10}\text{Cu}_{15}\text{Be}_{12.5}$, $\text{Mg}_{65}\text{Cu}_{25}\text{Gd}_{10}$ and $\text{Pd}_{43}\text{Ni}_{10}\text{Cu}_{27}\text{P}_{20}$ BMGs are studied by using the depth-sensing nanoindentation, macroindentation and uniaxial compression. A distinct plastic strain is observed in the $\text{Zr}_{52.5}\text{Al}_{10}\text{Ni}_{10}\text{Cu}_{15}\text{Be}_{12.5}$ BMG during uniaxial compression, while no global plastic deformation in $\text{Mg}_{65}\text{Cu}_{25}\text{Gd}_{10}$ and $\text{Pd}_{43}\text{Ni}_{10}\text{Cu}_{27}\text{P}_{20}$ BMGs. All the BMGs in the present study exhibit a loading rate dependency of serrated flow during nanoindentation, wherein the $\text{Zr}_{52.5}\text{Al}_{10}\text{Ni}_{10}\text{Cu}_{15}\text{Be}_{12.5}$ BMG shows a less prominent serrated flow with the lowest critical loading rate for the disappearance of the serration. The study of the deformation regions underneath a Vickers indenter reveals that the $\text{Zr}_{52.5}\text{Al}_{10}\text{Ni}_{10}\text{Cu}_{15}\text{Be}_{12.5}$ BMG exhibits a high number density of shear bands with the shear band spacing independent of the location. Whereas in the other two BMGs, especially in the $\text{Mg}_{65}\text{Cu}_{25}\text{Gd}_{10}$, the number density of shear bands is quite low and the shear band spacing depends strongly on the location. The difference in the plastic deformation behavior of the three BMGs can be explained a numerical calculation based on the free volume model.

Acknowledgments

Supported by the National Natural Science Foundation of China under Grant Nos. 10572142, 10432050, 50571109 and 10372103.

References

- [1] C.A. Schuh, A.C. Lund, T.G. Nieh, *Acta Mater.* 52 (2004) 5879.
- [2] A. Inoue, W. Zhang, T. Zhang, K. Kurosaka, *Acta Mater.* 49 (2001) 2645.
- [3] H.A. Bruck, T. Christman, A.J. Rosakis, W.L. Johnson, *Scr. Metall. Mater.* 30 (1994) 429.
- [4] R. Vaidyanathan, M. Dao, G. Ravichandran, S. Suresh, *Acta Mater.* 49 (2001) 3781.
- [5] K.M. Flores, R.H. Dauskardt, *Scr. Mater.* 41 (1999) 937.
- [6] L.Q. Xing, Y. Li, K.T. Ramesh, J. Li, T.L. Hafuagel, *Phys. Rev. B* 64 (2001) 180201.
- [7] W.J. Wright, R.B. Schwarz, W.D. Nix, *Mater. Sci. Eng. A* 319–321 (2001) 229.
- [8] K.M. Flores, R.H. Dauskardt, *Acta Mater.* 49 (2001) 2527.
- [9] W.H. Wang, C. Dong, C.H. Shek, *Mater. Sci. Eng. R* 44 (2004) 45.
- [10] X.K. Xi, D.Q. Zhao, M.X. Pan, W.H. Wang, Y. Wu, J.J. Lewandowski, *Phys. Rev. Lett.* 94 (2005) 125510.
- [11] R.J. Wang, F.Y. Li, J.F. Wang, W.H. Wang, *Appl. Phys. Lett.* 83 (2003) 2814.
- [12] J.J. Lewandowski, W.H. Wang, A.L. Greer, *Philos. Mag. Lett.* 85 (2005) 77.
- [13] U. Ramamurty, M.C. Kumaran, *Acta Mater.* 52 (2004) 181.
- [14] C.A. Schuh, T.G. Nieh, *J. Mater. Res.* 19 (2004) 46.
- [15] D.C.C. Lam, C.M.C. Arthur, *Mater. Sci. Eng. A* 318 (2001) 313.
- [16] T. Mukai, T.G. Nieh, Y. Kawamura, A. Inoue, K. Higashi, *Scr. Mater.* 46 (2002) 43.

- [17] S. Jana, U. Ramamurty, K. Chattopadhyay, Y. Kawamura, *Mater. Sci. Eng. A* 375–377 (2004) 1191.
- [18] W.H. Li, B.C. Wei, T.H. Zhang, L.C. Zhang, *Mater. Trans.* 46 (2005) 2954.
- [19] U. Harms, O. Jin, R.B. Schwarz, *J. Non-Cryst. Solids* 317 (2003) 200.
- [20] X.K. Xi, R.J. Wang, D.Q. Zhao, M.X. Pan, W.H. Wang, *J. Non-Cryst. Solids* 344 (2004) 105.
- [21] J. Schroers, W.L. Johnson, *Phys. Rev. Lett.* 93 (2004) 255506.
- [22] C.A. Schuh, T.G. Nieh, *Acta Mater.* 51 (2003) 87.
- [23] T. Benameur, K. Hajlaoui, A.R. Yavari, A. Inoue, B. Rezgui, *Mater. Trans.* 43 (2002) 2617.
- [24] F. Spaepen, *Acta Metall.* 25 (1977) 407.
- [25] Q. Yang, A. Mota, M. Ortiz, *Comput. Mech.* 37 (2006) 194.
- [26] D. Kramer, H. Huang, M. Kriese, J. Robach, J. Nelson, A. Wright, D. Bahr, W.W. Gerberich, *Acta. Mater.* 47 (1999) 333.